PNAS

**SUPPORTING INFORMATION**

# Reversible switching between two common protein folds in a designed system using only temperature

Tsega L. Solomon, Yanan He, Nese Sari, Yihong Chen, D. Travis Gallagher, Philip N. Bryan*, and John Orban*

*Email: pbryan@potomac-affinity-proteins.com, jorban@umd.edu

**This file includes:**

Figures S1 to S10

Tables S1 to S3

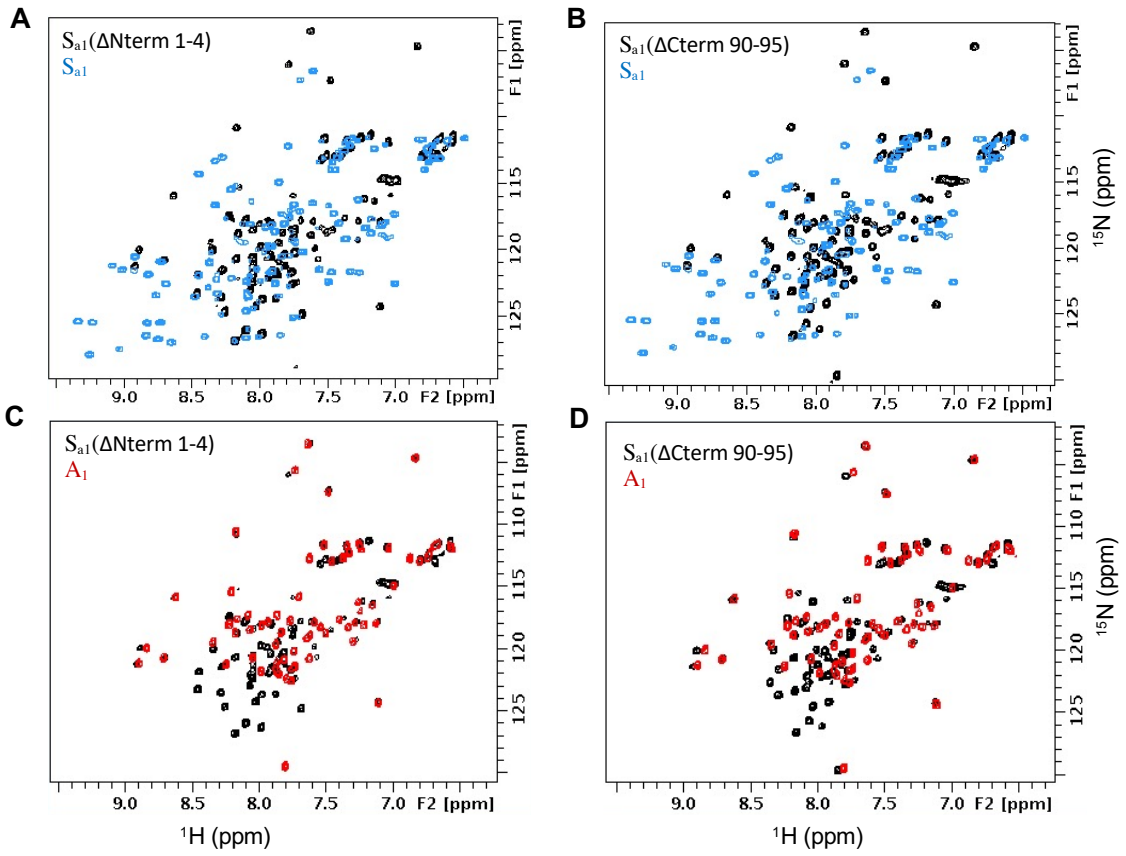


**Figure S1.** Unmasking of the alternate 3α fold with deletion mutations. **(A)** 2D $^{1}$H-$^{15}$N HSQC spectrum of $S_{a1}$(ΔNterm1-4) (*black*) overlaid with the spectrum of α/β-plait $S_{a1}$ (*blue*). **(B)** 2D $^{1}$H-$^{15}$N HSQC spectrum of $S_{a1}$(ΔCterm90-95) (*black*) overlaid with $S_{a1}$ (*blue*). **(C)** 2D $^{1}$H-$^{15}$N HSQC spectrum of $S_{a1}$(ΔNterm1-4) (*black*) overlaid with the spectrum of the 56 amino acid 3α-helical protein $A_1$ (*red*). **(D)** 2D $^{1}$H-$^{15}$N HSQC spectrum of $S_{a1}$(ΔCterm90-95) (*black*) overlaid with $A_1$ (*red*). All spectra were recorded at 5$^{o}$C.

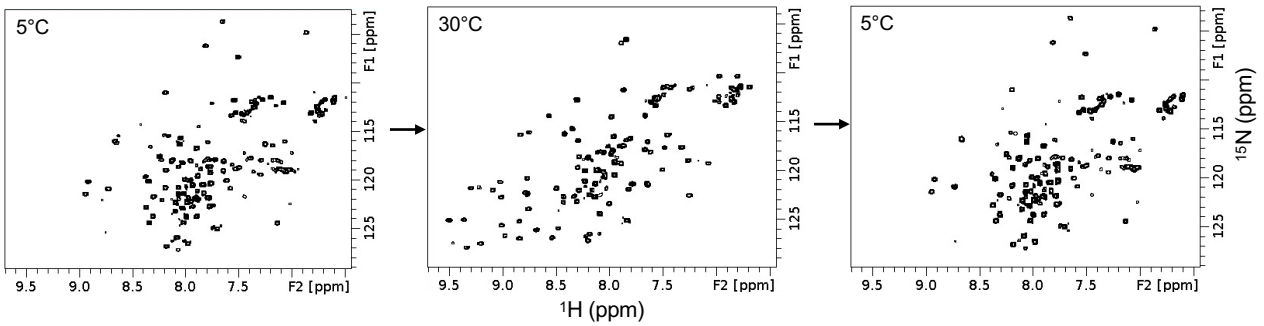


**Figure S2.** Reversibility of 3α to α/β-plait fold conversion. 2D $^{1}$H-$^{15}$N HSQC spectrum of $S_{a1}$V90T at 5°C (*left*) before raising the temperature to 30°C (*center*), followed by a spectrum at 5°C (*right*) after acquisition of the 30°C spectrum. Samples equilibrated within the time required (<10 min) for tuning, shimming, and acquisition of the first FID.

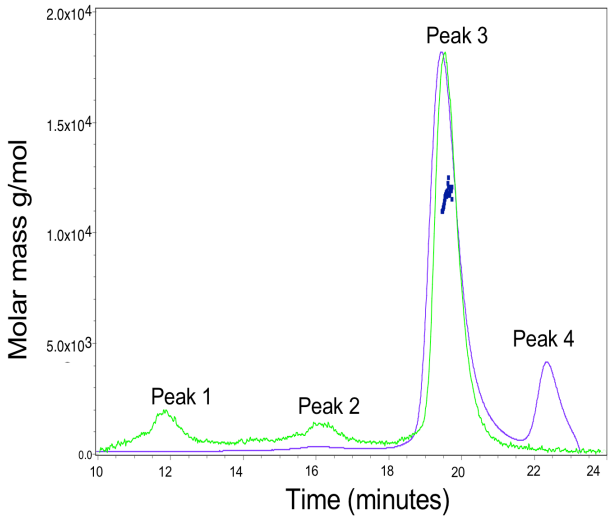


**Figure S3.** Oligomeric state of $S_{a1}$V90T. Size exclusion and multi-angle static light scattering analysis of $S_{a1}$V90T at 22°C. Light scattering (*green*) and the derivative of the refractive index (*purple*) are displayed as a function of retention time. Peak 1 represents the void peak of the column. Peak 2 is a standard calibration peak of bovine serum albumin (68 kDa). Peak 3, where the light scattering and refractive index traces coincide, represents the $S_{a1}$V90T sample having a monodispersed, derived molecular weight of 11.1 kDa (*blue*). This is within 6% error of the monomeric molecular weight calculated based on the amino acid sequence. Peak 4 in the refractive index trace is a buffer mismatch artifact.

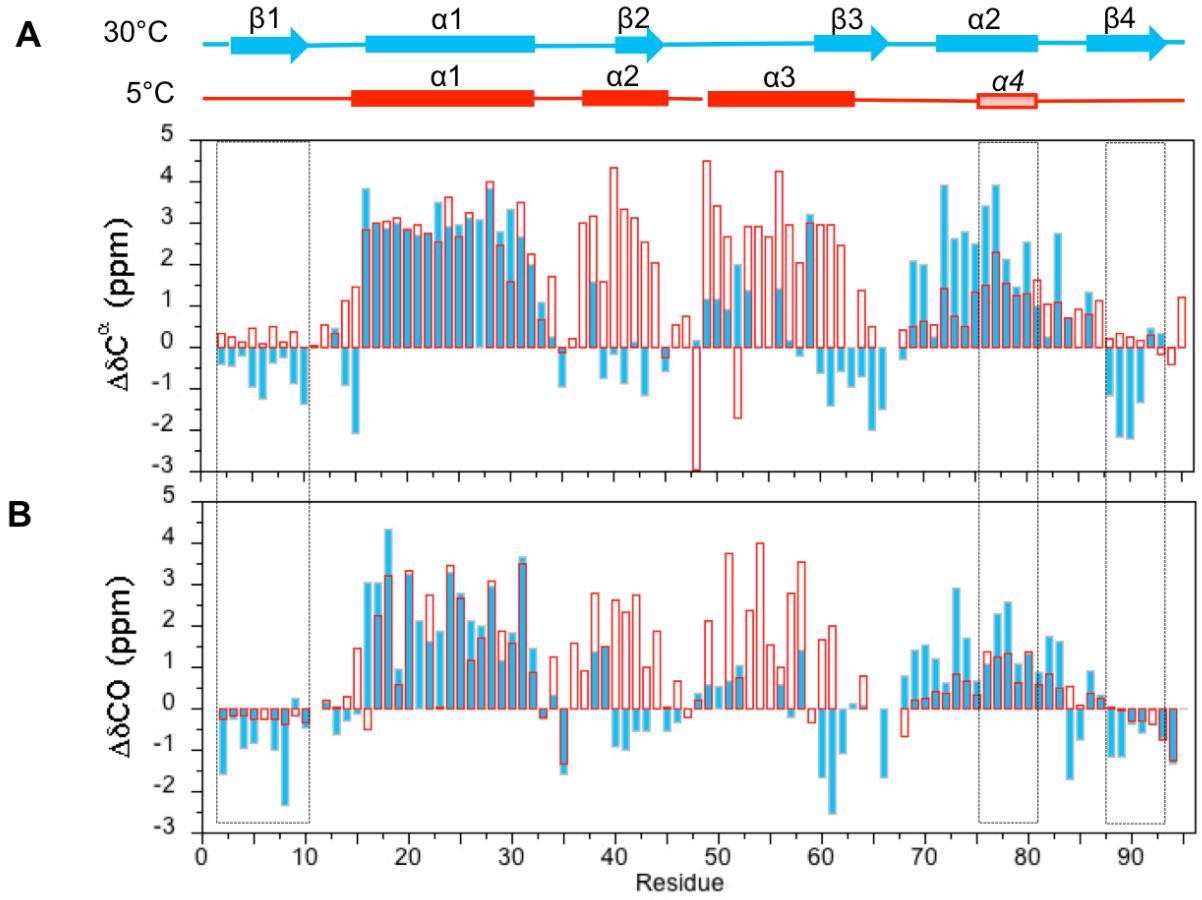


**Figure S4.** Secondary chemical shift analysis for $S_{a1}$V90T as a function of temperature. (**A)** Backbone Cα chemical shift differences between measured and calculated random coil values of $S_{a1}$V90T at 5°C (*red*) and 30°C (*cyan*). (**B**) Corresponding backbone CO chemical shift differences. Highlighted regions show extent of propensity for the alternate conformation in the N- and C-terminal ends of $S_{a1}$V90T.

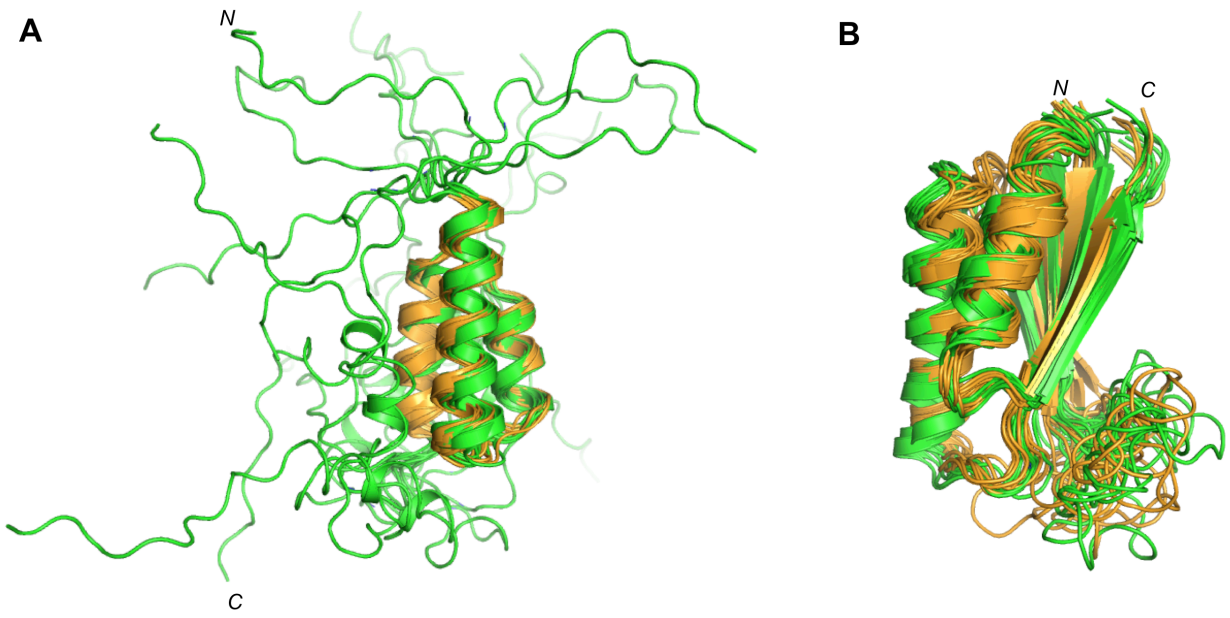


**Figure S5.** Comparison of $S_{a1}$V90T structures at 5°C and 30°C with the parent folds, $A_1$ (3α) and $S_{a1}$ (α/β-plait). **(A)** The ensemble of 95-residue $S_{a1}$V90T structures at 5°C (green) is overlaid with the ensemble of 56-residue $A_1$ structures (PDBDev 00000083[15], orange). The average backbone RMSD over the corresponding 3α regions is 0.4Å. **(B)** The ensemble of $S_{a1}$V90T structures at 30°C (green) overlaid with the $S_{a1}$ ensemble (PDB 7MN1[15], orange). The average backbone RMSD over ordered regions is 0.9Å.

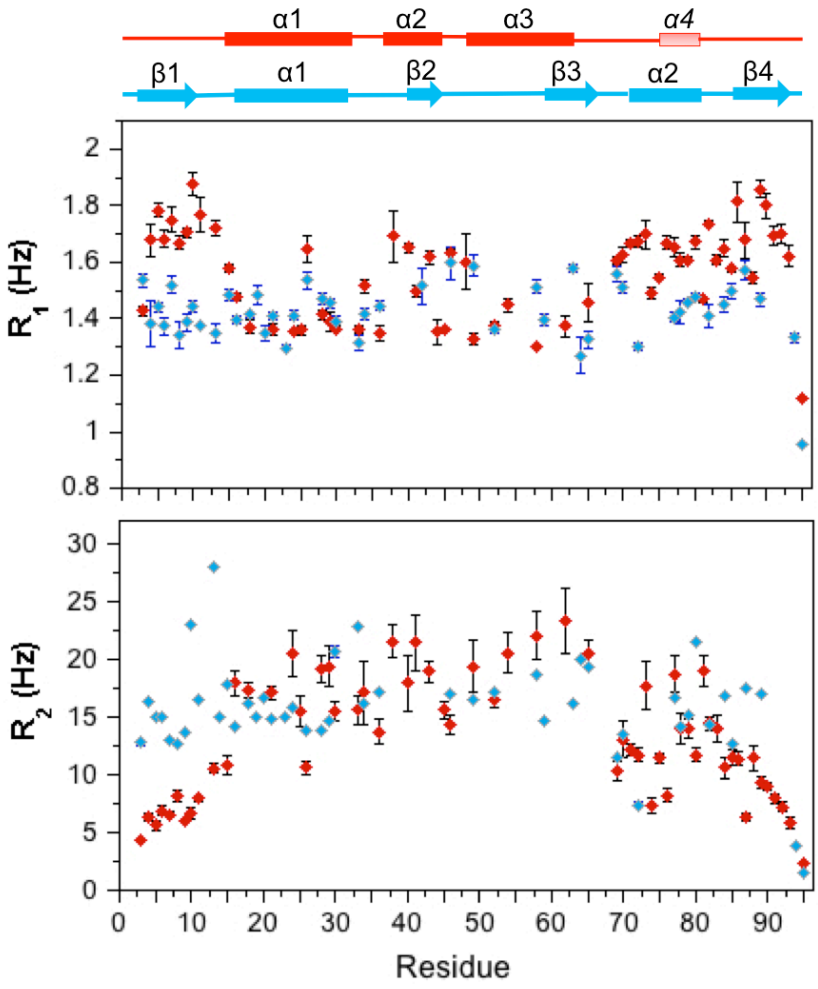


**Figure S6.** Backbone dynamic characterization of $S_{a1}$V90T at 17°C. $^{15}$N-$R_1$ and $^{15}$N-$R_2$ rates for $S_{a1}$V90T where 3α (red) and α/β-plait (blue) forms are equally populated. The errors for the α/β-plait $R_2$ values are within the data point markers.

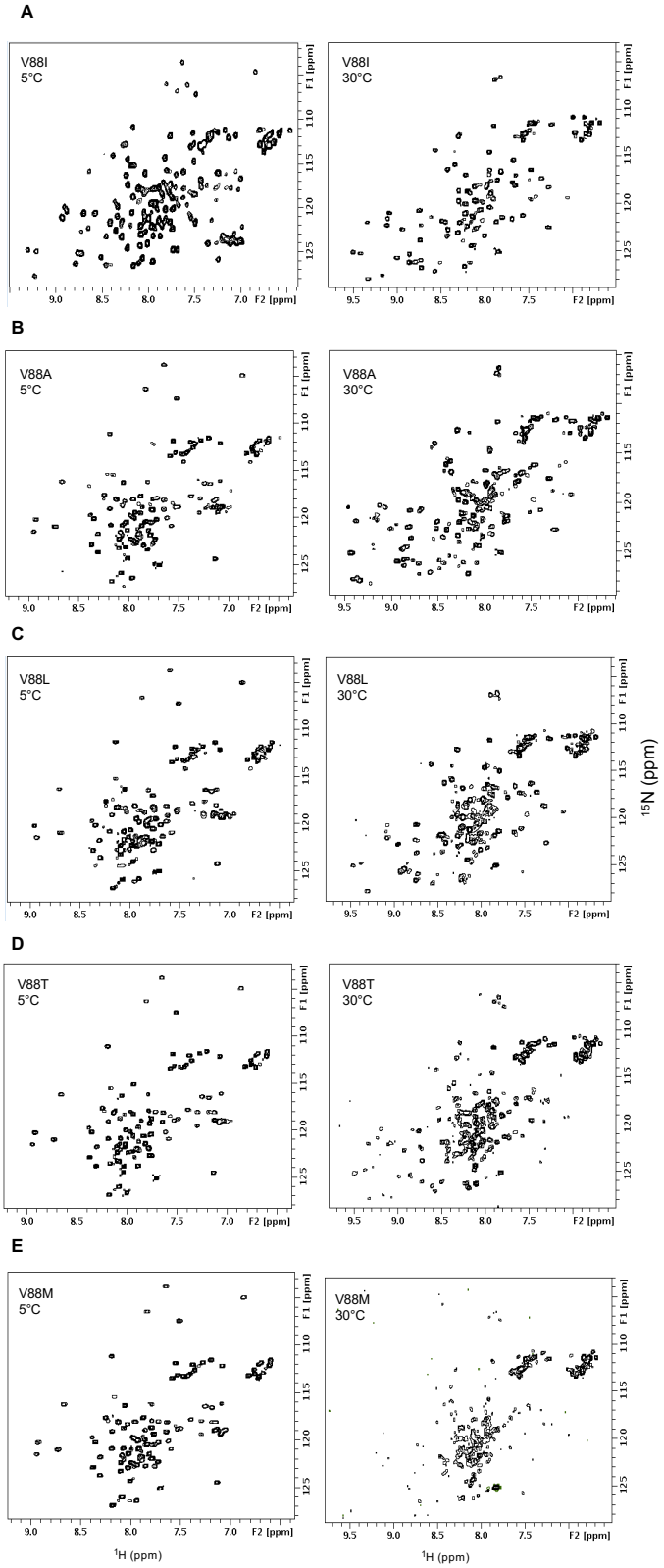


**Figure S7.** Conformational analysis of $S_{a1}$V88X mutants. 2D $^{1}$H-$^{15}$N HSQC spectra of $S_{a1}$ mutants V88I (A), V88A (B), V88L (C), V88T (D), and V88M (E) at 5°C (*left*) and 30°C (*right*).

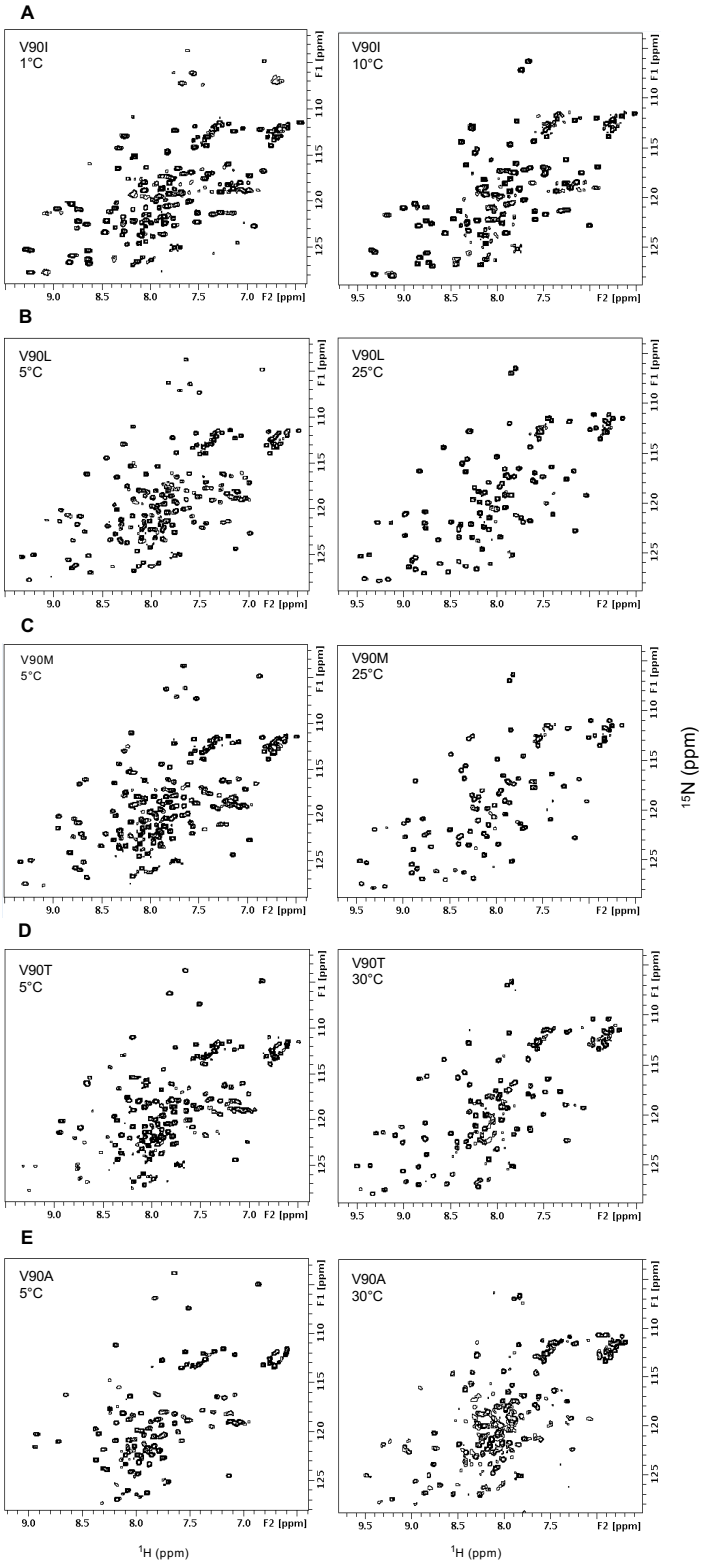


**Figure S8.** Conformational analysis of $S_{a1}$V90X mutants. 2D $^{1}$H-$^{15}$N HSQC spectra of $S_{a1}$ mutants V90I (A), V90L (B), V90M (C), V90T (D), and V90A (E) at 1 or 5°C (*left*) and 10, 25 or 30°C (*right*).

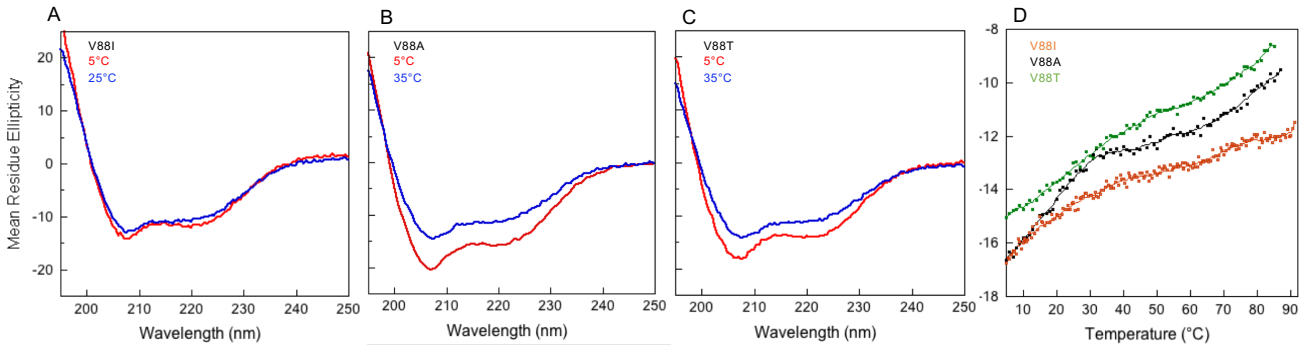


**Figure S9.** Analysis of conformation and thermal denaturation by CD. Mean residue ellipticity versus wavelength is plotted for **(A)** V88I at 5°C and 25°C, (**B**) V88A at 5°C and 35°C, and (**C**) V88T at 5°C and 35°C using a 1 mm path length cuvette with 5 μM protein sample. (**D**) Mean residue ellipticity is plotted versus temperature for the three V88 mutants in the range from 5 to 90°C. The increase in ellipticity at 222 nm for $S_{a1}$V88T at high temperature indicates less secondary structure than for V88A, leading to an approximate order of V88I>V88A>V88T α/β-plait stability.

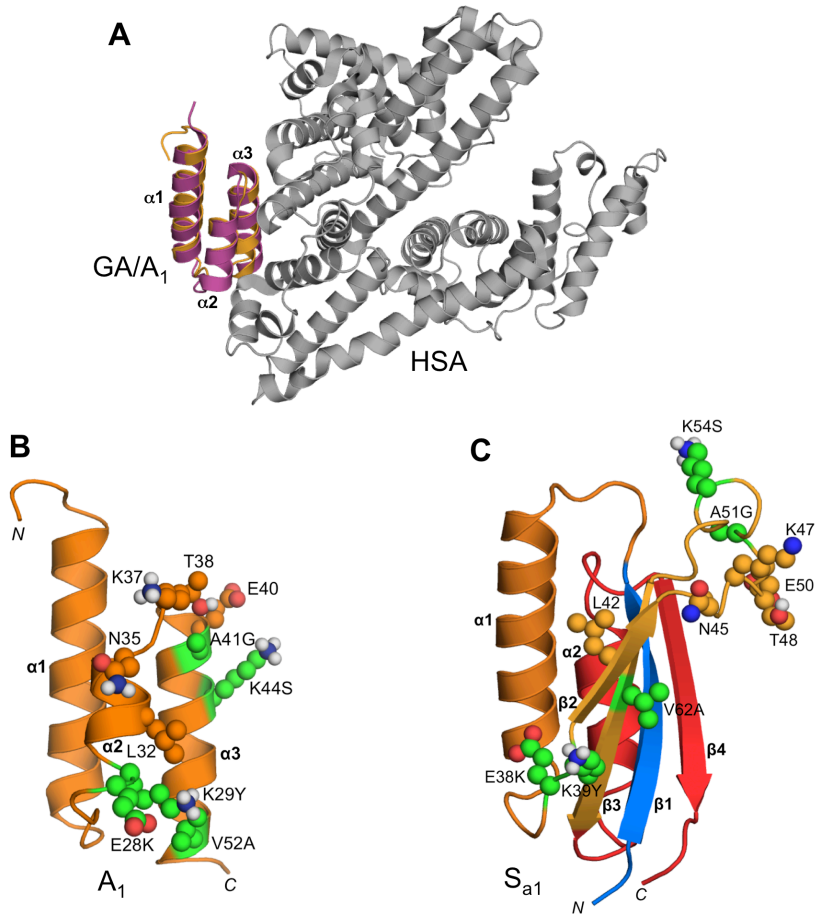


**Figure S10.** Engineering HSA-binding function into $A_1$ and $S_{a1}$. **(A)** The structure of $A_1$ (*orange*) is aligned with wild-type GA (*magenta*) bound to HSA (*gray*), PDB 1TF0. **(B)** NMR structure of $A_1$[15] showing the HSA binding site residues in sphere representation. **(C)** NMR structure of $S_{a1}$[15] showing positions of HSA binding site residues in sphere representation. Those in orange (L42, N45, K47, T48, and E50) are already present in $A_1$ and $S_{a1}$ while those in green (E38K, K39Y, A51G, K54S, and V62A) were introduced by site directed mutagenesis.

**Table S1.** Summary of structure statistics.

| | $S_{a1}$V90T, 5°C | $S_{a1}$V90T, 30°C |
|---|---|---|
| *A. Experimental restraints* | | |
| NOE restraints | | |
| Intraresidue | | 50 |
| Sequential (\|i-j\| =1) | | 74 |
| Medium-range (1<\|i-j\|≤5) | | 72 |
| Long-range (\|i-j\|>5) | | 31 |
| Hydrogen bond restraints | | 83 |
| Total NOE restraints | | 310 |
| CS-Rosetta input | | |
| $^{13}C^{\alpha}$ shifts | 90 | 90 |
| $^{13}C^{\beta}$ shifts | 79 | 85 |
| $^{13}CO$ shifts | 86 | 82 |
| $^{15}N$ shifts | 87 | 83 |
| $^{1}H^{N}$ shifts | 87 | 83 |
| $^{1}H^{\alpha}$ shifts | 41 | 39 |
| *B. Secondary structure RMSDs to the mean structure (Å)*[a] | | |
| Backbone atoms | 0.90 ± 0.45 | 1.15 ± 0.31 |
| Heavy atoms | 1.59 ± 0.48 | 1.81 ± 0.35 |
| *C. Measures of structure quality (%)* | | |
| Ramachandran distribution | | |
| Most favored | 94.50 ± 2.20 | 92.55 ± 2.49 |
| Additionally allowed | 5.00 ± 2.20 | 7.22 ± 2.42 |
| Generously allowed | 0.34 ± 0.70 | 0.11 ± 0.35 |
| Disallowed | 0 | 0.11 ± 0.35 |
| Bad contacts | 1.20 ± 0.80 | 0.50 ± 0.71 |
| Overall dihedral G factor | 0.37 ± 0.05 | 0.28 ± 0.02 |
| *D. PDB/BMRB codes* | | |
| PDB/PDBDev | 00000132 | 8E6Y |
| BMRB | 51338 | 51339 |

[a] Stable secondary structure regions used were as follows: At 5°C, residues 15-32, 37-45, and 49-63; at 30°C, residues 3-10, 16-32, 40-44, 60-66, 72-81, and 86-92.

**Table S2.** Temperature dependence of correlation times ($\tau_C$, ns) for $S_{a1}$V90T regions.

| | $\tau_c$ (5°C) | $\tau_c$ (17°C) | $\tau_c$ (30°C) |
|---|---|---|---|
| 3-α[a] | 16.5 | 10.6 | - |
| α4[b] | 11.0 | 8.7 | - |
| N-terminus[c] | 5.5 | 5.4 | - |
| C-terminus[d] | 7.7 | 6.7 | - |
| α/β-plait[e] | - | 9.8 | 6.7 |

[a] Residues 10-66; [b] residues 75-81; [c] residues 1-10; [d] residues 67-95; [e] residues 2-95. Correlation times are obtained from equation 2 using the average $T_1$ and $T_2$ values corresponding to each region.

**Table S3.** Exchange rate constants from ZZ-exchange spectroscopy.[a]

| Temperature | Residue[b] | $K_{eq}$ | $k_{\alpha/\beta \rightarrow 3\alpha}$ ($s^{-1}$) | $k_{3\alpha \rightarrow \alpha/\beta}$ ($s^{-1}$) |
|---|---|---|---|---|
| 10°C | Q16 | 0.77 | 0.7 ± 0.2 | 0.6 ± 0.1 |
| | G34 | 0.45 | 1.2 ± 0.3 | 0.5 ± 0.1 |
| | G58 | 0.35 | 1.6 ± 0.4 | 0.6 ± 0.1 |
| | **Mean** | **0.52** | **1.2. ± 0.3** | **0.6 ± 0.1** |
| 17°C | Q16 | 1.48 | 1.0 ± 0.1 | 1.4 ± 0.2 |
| | G34 | 1.19 | 1.3 ± 0.3 | 1.6 ± 0.4 |
| | G58 | 1.05 | 1.4 ± 0.3 | 1.5 ± 0.3 |
| | **Mean** | **1.24** | **1.2 ± 0.2** | **1.5 ± 0.3** |
| 24°C | Q16 | 2.33 | 1.4 ± 0.3 | 3.3 ± 0.7 |
| | G34 | 2.67 | 1.6 ± 0.4 | 4.0 ± 0.9 |
| | G58 | 2.53 | 1.3 ± 0.3 | 3.4 ± 0.7 |
| | **Mean** | **2.51** | **1.4 ± 0.3** | **3.6 ± 0.8** |

[a] Exchange rates were determined from equation 4 as described in the Materials and Methods section. [b] Residues Q16, G34, and G58 were chosen due to their well-resolved cross-peaks and auto-peaks.